Magnetization process of the layered diluted ferromagnetic semiconductor (Ba,K)(Zn,Mn)$_2$As$_2$ studied by x-ray magnetic circular dichroism

Yuxuan Wan,[1,2] Guoqiang Zhao,[3] Goro Shibata,[1,4] Keisuke Ikeda,[1] Masahiro Suzuki,[1] Masaki Kobayashi,[5] Shoya Sakamoto,[1] Zheng Deng,[3] Kan Zhao,[3] Bijuan Chen,[3] Yukiharu Takeda,[4] Tetsuo Okane,[4] Yuji Saitoh,[4] Hiroshi Yamagami,[4,6] Yasutomo J. Uemura,[7] Changqing Jin,[3] and Atsushi Fujimori[1,8,*]

[1]*Department of Physics, The University of Tokyo, Bunkyo-ku, Tokyo 113-0033, Japan*
[2]*Institute for Solid State Physics, The University of Tokyo, Kashiwa, Chiba 277-8581, Japan*
[3]*Beijing National Laboratory for Condensed Matter Physics, and Institute of Physics, Chinese Academy of Sciences, Beijing 100190, China*
[4]*Materials Sciences Research Center, Japan Atomic Energy Agency, Sayo, Hyogo 679-5148, Japan*
[5]*Department of Electrical Engineering and Information Systems, The University of Tokyo, Bunkyo-ku, Tokyo 113-0033, Japan*
[6]*Department of Physics, Kyoto Sangyo University, Kita-Ku, Kyoto 603-8555, Japan*
[7]*Department of Physics, Columbia University, New York, New York 10027, USA*
[8]*Department of Physics, National Tsing-Hua University, Hsinchu 300044, Taiwan*

(Received 26 October 2025; revised 12 March 2026; accepted 7 April 2026; published 4 May 2026)

The layered 122-type diluted ferromagnetic semiconductor (Ba,K)(Zn,Mn)$_2$As$_2$ has attracted much attention both for its high Curie temperature up to ∼230 K and for the independent control of charge-carrier and spin concentrations through doping K and Mn atoms at the Ba and Zn sites, respectively. In order to unveil the nature of the ferromagnetism in (Ba,K)(Zn,Mn)$_2$As$_2$, its magnetization process has been studied by x-ray magnetic circular dichroism (XMCD) at the Mn $L_{2,3}$ edge in a wide range of temperature and magnetic field. The average magnetization of the Mn atoms as a function of magnetic field (M–H curves) at various temperatures could be successfully explained by a mixture of paramagnetic (PM), superparamagnetic (SPM), and ferromagnetic (FM) components as previously reported for GaMnAs, revealing the complex nature of the ferromagnetism in (Ba,K)(Zn,Mn)$_2$As$_2$. The average magnetization of the SPM clusters of different sizes and the FM regions were found to be small compared to those in GaMnAs, which we attribute to the antiferromagnetic interaction between nearest-neighbor Mn atoms in (Ba,K)(Zn,Mn)$_2$As$_2$ on the basis of recent theoretical predictions.

DOI: 10.1103/69sm-fz7z

I. INTRODUCTION

Spintronics, which utilize both the spin and charge degrees of freedom in electronic devices, is a promising field of future technology [1,2]. Like semiconductors for electronics, magnetic semiconductors are key materials for spintronics [3,4]. In particular, diluted ferromagnetic semiconductors (FMSs) are candidate materials for nonvolatile memories and logic switches. Historically, the most extensively studied FMSs are Mn-doped III-V semiconductors such as InMnAs [5] and GaMnAs [6–8]. In the III-V based FMSs, Mn^{2+} ions act as acceptors providing the system with both holes and spins. There are two models to explain the origin of the ferromagnetism in the FMSs: One is the *p-d* Zener model, which is based on mean-field theories and treats the charge carriers doped in the host valence bands as itinerant ones exchange-coupled with the Mn^{2+} local spins [9–13]; the other is the impurity-band (IB) model, where the holes are weakly bound by the magnetic impurities through exchange interaction, form magnetic polarons, and hop between the impurity sites via double-exchange mechanism [14–18].

The Mn-doped III-V FMSs have the following disadvantages. The substitution of divalent Mn ions at the trivalent Ga sites, i.e., the heterovalent substitution, severely limits chemical solubility and, therefore, a sufficient amount of Mn can be introduced only in thin films grown by molecular-beam epitaxy [19]. Furthermore, since the doped Mn ions provide both the hole carriers and the spins, the transport and magnetic properties cannot be controlled independently. The Mn doping also entails uncontrollable As antisite defects as well as interstitial Mn, leading to the difficulty in controlling the carrier density of the system [20,21]. Due to those limitations of the Mn-doped III-V FMSs, another platform has been anticipated from both practical device applications and basic science points of view.

Recently, Zhao *et al.* [22] successfully synthesized a new kind of FMS: 122-type (Ba,K)(Zn,Mn)$_2$As$_2$ in the bulk form, which exhibits *p*-type electrical conductivity. It has the tetragonal $ThCr_2Si_2$-type structure and is isostructural to the 122-type iron-based superconductors such as carrier-doped $BaFe_2As_2$ [23], as shown in Fig. 1(a). The 122 FMSs have a high Curie temperature (T_C) exceeding ∼230 K, which is higher than the T_C of other Mn-doped FMSs [22,24]. The host compound $BaZn_2As_2$ has two substituted sites: Ba and Zn. The carrier and spin densities can be controlled independently by the doping levels of K and Mn, respectively, unlike the

*Contact author: fujimori@phys.s.u-tokyo.ac.jp

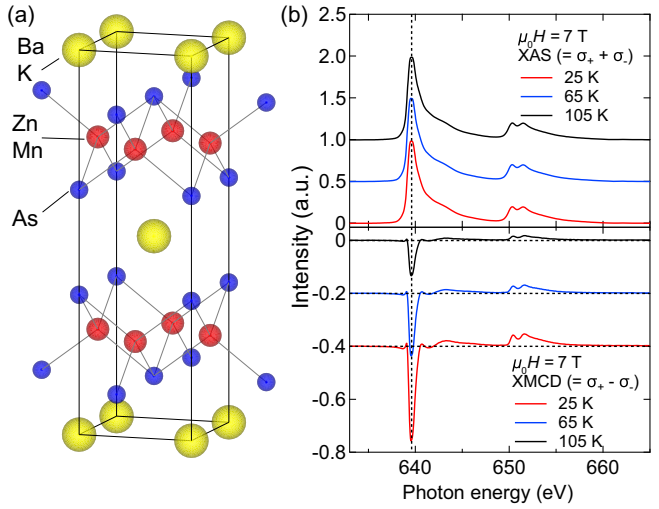

FIG. 1. (a) Crystal structure of $(Ba,K)(Zn,Mn)_2As_2$. (b) X-ray absorption (XAS) and x-ray magnetic circular dichroism (XMCD) spectra at the Mn $L_{2,3}$ edge of $(Ba_{0.904}K_{0.096})(Zn_{0.805}Mn_{0.195})_2As_2$ measured at $\mu_0H = 7$ T. The small positive feature near 645 eV is a characteristic signature of Mn^{2+} XMCD spectra [8].

III-V-based FMSs. Hole carriers are introduced by K doping at the Ba sites, and magnetic moments are introduced by Mn doping at the Zn sites. Due to the same valences of Zn and Mn, the Mn concentration can be made as high as 0.195 in bulk crystal [24]. In addition, interstitial Mn ions are energetically precluded [25]. Further progress has been made by Peng *et al.* [26], who successfully increased the T_C of $(Ba,K)(Zn,Mn)_2As_2$ to 260 K by enhancing the Mn concentration in combination with parallel K doping. Their study revealed that a sufficient carrier concentration suppresses the short-range antiferromagnetic interaction between the nearest-neighbor Mn-Mn pairs, thereby strengthening the ferromagnetism. These findings highlight a promising strategy for achieving room-temperature ferromagnetism in diluted magnetic semiconductors. Suzuki *et al.* performed resonant photoemission spectroscopy (RPES) measurements on $(Ba,K)(Zn,Mn)_2As_2$, and proved that the Mn 3*d* electrons are basically localized and that the Mn ions are in the 2+ valence state [27]. Angle-resolved photoemission spectroscopy (ARPES) and resonant inelastic x-ray scattering (RIXS) measurements were also performed by Suzuki *et al.* [28,29]. The ARPES study revealed Fermi surfaces of the host $BaZn_2As_2$ bands doped with hole carriers, in addition to the formation of the impurity bands, resulting from strong hybridization between the Mn 3*d* and As 4*p* orbitals [28]. Sakamoto *et al.* studied the magnetic anisotropy with angle-resolved x-ray magnetic circular dichroism (XMCD) experiments [30].

On the other hand, the magnetism of $(Ba,K)(Zn,Mn)_2As_2$ is complex and far from trivial to understand. In particular, the saturation magnetization is too small (0.5–1.0 μ_B/Mn) [24,29,30] compared to the full moment of the Mn^{2+} ion (5μ_B/Mn). The temperature and magnetic-field dependences of the magnetization of $(Ba,K)(Zn,Mn)_2As_2$ are expected to provide important information about the origin of the complex magnetism of this material. X-ray absorption spectroscopy (XAS) and XMCD measurements of the magnetization process are useful techniques to reveal the nature of ferromagnetism in FMSs [31,32]. A theoretical study beyond mean-field theory attempted to explain the complex magnetic properties in $(Ba,K)(Zn,Mn)_2As_2$ [25]. Studies on the magnetization process are expected to reveal the theoretically predicted complex nature of the ferromagnetism.

In the present paper, we use XMCD to study the magnetization process of Mn 3*d* electrons in $(Ba,K)(Zn,Mn)_2As_2$ in a wide temperature and magnetic field range. By analyzing the magnetization curves (*M*–*H* curves) at various temperatures both above and below T_C, we successfully fit the experimental results using a model consisting of the ferromagnetic, superparamagnetic, and paramagnetic components, and unveil the complex nature of ferromagnetism in $(Ba,K)(Zn,Mn)_2As_2$.

TABLE I. Spin and orbital magnetic moments, m_{spin} and m_{orb}, deduced by applying the XMCD sum rules to the experimental results. m_{spin} and m_{orb} have experimental uncertainties of ±20% and ±10%, respectively, and the ratio m_{orb}/m_{spin} has an uncertainty of ∼ ± 25%. The uncertainties are estimated systematic uncertainties reflecting variations in background subtraction, edge-step normalization, and integration limits, rather than statistical standard deviations.

Temperature (K)	m_{orb}/m_{spin}	$m_{orb}(\mu_B/Mn)$	$m_{spin}(\mu_B/Mn)$
25	0.106	0.122	1.12
65	0.087	0.063	0.72
105	0.071	0.028	0.40

II. EXPERIMENT

Single crystals of $(Ba_{0.904}K_{0.096})(Zn_{0.805}Mn_{0.195})_2As_2$ were synthesized by the flux method as described in Ref. [24]. Crystal structure is shown in Fig. 1(a). The Curie temperatures of the samples were ∼60 K. The XMCD measurements were carried out at beamline BL23SU of SPring-8 [33]. The range of photon energy was 620–680 eV with the energy resolution of $E/\Delta E > 10\,000$. The beam size was less than 0.2 mm in diameter. The samples were cleaved at $T = 10$ K in an ultrahigh vacuum of 10^{-9} Torr. The measurement temperature ranged from 20 to 200 K, and the magnetic field which ranged from −7 to 7 T was applied along the *c* axis, which is the easy axis of $(Ba,K)(Zn,Mn)_2As_2$. The total-electron-yield (TEY) mode was used to detect XAS and XMCD signals with high S/N ratio. Although the TEY mode is considered to be relatively surface sensitive, the probing depth is on the order of nm, which is sufficiently large to study the bulk magnetic properties. The directions of the incident x-rays and magnetic field were perpendicular to the sample surfaces (the *ab* plane). For the *M*–*H* loops we employed the normalized Mn L_3-edge XMCD integrated intensity as a proxy of the Mn-specific magnetization at each (T, H) point, which preserves the relative field/temperature dependences with a stable S/N under limited beam time. Full $L_3 + L_2$ integrations were used for the sum-rule evaluation in Table I.

III. RESULTS AND ANALYSIS

XAS and XMCD spectra of $(Ba_{0.904}K_{0.096})(Zn_{0.805}Mn_{0.195})_2As_2$ are shown in Fig. 1(b). At all temperatures,

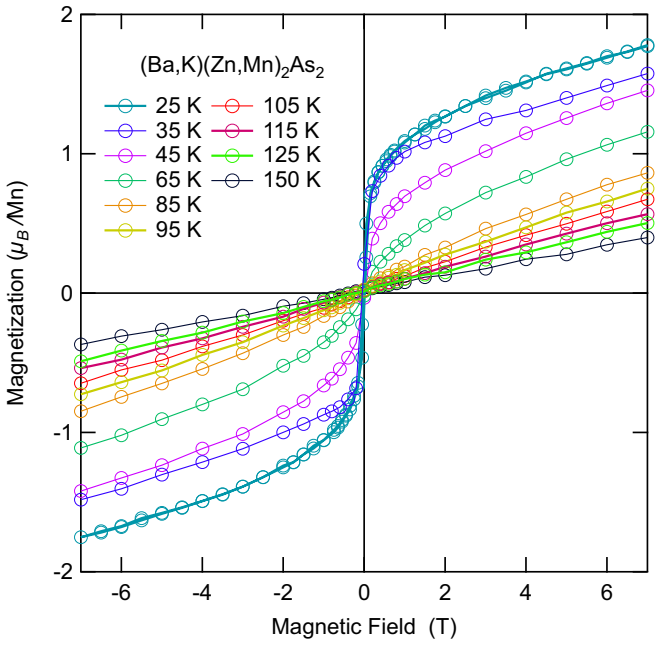

FIG. 2. M–H curves at various temperatures of $(Ba_{0.904}K_{0.096})(Zn_{0.805}Mn_{0.195})_2As_2$ obtained from the H dependence of the XMCD intensity at the Mn L_3 edge.

the XAS spectra exhibit the same line shapes and intensities. The XMCD spectra also show temperature-independent line shapes but their intensity increases with decreasing temperature. The XAS and XMCD spectra have been normalized to the intensities of the XAS L_3 peaks averaged for the two circular polarizations. The broad but obvious multiplet structures of the Mn $L_{2,3}$ edge show that the Mn $3d$ electrons are in the localized d^5 configuration, as shown by the RPES and RIXS measurements [27,29]. Table I shows the temperature dependence of the spin and orbital magnetic moments ($m_{\rm spin}$ and $m_{\rm orb}$) deduced using the XMCD sum rules. Here, the hole number of 5 and the correction factor of 1.47 for the spin sum rules are assumed [34]. The table indicates that both the spin and orbital magnetic moments decrease as the temperature increases, while the ratio $m_{\rm orb}/m_{\rm spin}$ remains largely unchanged within experimental uncertainties.

The M–H curves of the $(Ba,K)(Zn,Mn)_2As_2$ samples derived from the Mn L_3-edge XMCD intensities using the XMCD sum rules at varied temperatures are shown in Fig. 2. The field/temperature dependences observed by XMCD are consistent with trends reported for bulk magnetization in related 122 compounds above ∼10–20 K (linear high-field tails with weak hysteresis). XMCD isolates the Mn $3d$ contribution and avoids global offsets (e.g., diamagnetic backgrounds) present in SQUID/VSM. At temperatures far above $T_{\rm C}$, the M–H curves are almost linear, indicating paramagnetism. As the temperature decreases, the curves show a nonlinear H dependence: the curves are convex at low magnetic fields, and recover the linear behavior at high magnetic fields. The convex H dependence at low magnetic fields is a characteristic of superparamagnetism, and the linear increase at high H suggests the existence of paramagnetic Mn spins co-existing with the superparamagnetic clusters. Within our measurement window (25 K to 150 K), we observed no noticeable hysteresis in the XMCD M–H loops. This implies that the blocking/stabilization temperature of the SPM clusters lies below our window, consistent with reports that clear hysteresis appears only at ∼2 K and quickly vanishes upon warming [22]. Below $T_{\rm C}$, the magnetization shows a nonzero value down to $H \sim 0$, which indicates the existence of ferromagnetism. The hysteresic behavior is negligible in Fig. 2, however, because the hysterisis was observed only at 2 K when $H \parallel c$ axis [22]. In the following, we analyze the M–H curves at various temperatures using a model in which different types of magnetic components coexist and contribute to the overall magnetization. Although the magnetization processes in other FMSs have been studied by similar methods [31,32], the analysis of M–H curves below $T_{\rm C}$ has been still difficult and controversial. Here, we improve the method by considering large clusters containing a high concentration of Mn ions to be either superparamagnetic (SPM) or ferromagnetic (FM), while isolated Mn ions are considered to be paramagnetic (PM). Additionally, we take into account the possibility that there are antiferromagnetically coupled nearest-neighbor Mn pairs or nonmagnetic (NM) Mn ions which have negligible contributions to the M–H curve. To quantify this situation, the M–H curves are fitted using the following equations [32]:

$$M[\mu_B/\mathrm{Mn}] = aL(b\mu_0 H) + c\mu_0 H + d, \tag{1}$$

$$L(x) = \coth(x) - 1/x, \tag{2}$$

$$a = M_{\rm FM} P_{\rm SPM}, \tag{3}$$

$$b = \mu/k_{\rm B}T, \tag{4}$$

$$d = M_{\rm FM} P_{\rm FM}. \tag{5}$$

The first term on the right-hand side of Eq. (1) represents the contribution of SPM clusters, described by the Langevin function $L(x)$ defined in Eq. (2). This term reflects the average magnetization properties of SPM clusters, rather than employing multiple Langevin functions for clusters of different sizes, which would complicate the determination of the macroscopic magnetic properties of the material. The second term accounts for the paramagnetic contribution, which varies linearly with the applied magnetic field H. The third term represents the contribution of ferromagnetism. Above $T_{\rm C}$, the long-range FM contribution vanishes in our model framework. Below $T_{\rm C}$, the FM component is treated as an effectively saturated contribution within the experimental magnetic-field window, since the magnetic field required to saturate the FM magnetization is much smaller than the field range used in the present measurements. Therefore, the FM contribution can be approximated as a field-independent offset in the present analysis. In the vicinity of $T_{\rm C}$, deviations from simple linear field dependence are effectively captured by the Langevin term, which represents the nonlinear magnetization associated with correlated Mn moments or magnetic clusters. The parameter a in Eq. (3) represents the product of the average magnetization per Mn ion $M_{\rm FM}$ in the FM and SPM regions and the fraction $P_{\rm SPM}$ of Mn ions in the SPM state; b is related to the average total magnetic moment of the SPM Mn clusters μ and the

temperature T via $b = \mu/k_B T$; and d is the product of M_{FM} and the fraction P_{FM} of Mn ions in the FM state.

Now we discuss parameter c which characterizes the PM contribution. The PM component below the Curie temperature T_C is attributed to isolated Mn ions [31]. We assume the Curie law to describe the PM contribution, as follows:

$$c = \chi_{PM} = C_{ion} P_{iso}/T, \tag{6}$$

where χ_{PM} is the susceptibility of the PM state, C_{ion} is the ionic value of the Curie constant, and P_{iso} is the fraction of isolated Mn ions that contribute to the PM state. The theoretical value of the Curie constant is given by

$$C_{ion} = \frac{\mu_0 \mu_B^2}{3k_B} N g_J^2 J(J+1) = 7.83, \tag{7}$$

where μ_0 denotes the vacuum permeability, μ_B the Bohr magneton, k_B the Boltzmann constant, N the number of magnetic atoms, and g_J the Landé g factor. For the Mn^{2+} ion, $J = 5/2$ and $g_J = 2$ because the orbital magnetic moment is almost quenched. It should be noted that the Mn $L_{2,3}$-edge XMCD signals do not contain contributions from the band g factor.

Above T_C, the PM contribution arises from both the isolated Mn ions and those newly formed by the fragmentation of the FM and SPM regions, and can be described by the Curie-Weiss law:

$$c = \chi_{PM} = C_{ion} P_{iso}^{55K}/T + C_{ion} P_{CW}/(T - T_C), \tag{8}$$

where P_{iso}^{55K} is the fraction of the isolated Mn ions at 55 K just below T_C, and P_{CW} is the fraction of the newly formed PM Mn^{2+} ions. Thus, the fraction of PM Mn ions is given by

$$P_{PM} = P_{iso}^{55K} + P_{CW}. \tag{9}$$

Now we estimate an appropriate value of the ferromagnetic moment M_{FM} from the present data. Previous studies on $(Ba,K)(Zn,Mn)_2As_2$ indicate that most of the Mn ions are in the Mn^{2+} state, which means that the ferromagnetic moment would be $5\mu_B$ per Mn if all the Mn spins were aligned in the same direction [27]. However, a theoretical study beyond mean-field theory [25] suggests that the average ferromagnetic moment M_{FM} may be reduced by the short-range antiferromagnetic (AFM) coupling between nearest-neighbor Mn ions. In order to estimate an appropriate M_{FM} value, the minimum value of M_{FM} can be given using the relation

$$P_{FM} + P_{PM} + P_{SPM} < 1. \tag{10}$$

At a temperature of 25 K, the minimum value of M_{FM} is calculated to be approximately $1.7\mu_B$. Considering this constraint, along with previous magnetization measurements [22] and the present XMCD results (Table I), we adopt a strongly reduced value of $M_{FM} \sim 2\mu_B$ in the present fitting procedure for the M–H curves. It should be noted that M_{FM} may be temperature dependent. Fitting results for other values of M_{FM} are presented in the Appendix. These results demonstrate that, while the absolute values of the extracted model parameters are influenced by M_{FM}, the overall trends remain unchanged. Specifically, the evolution of magnetic clusters—from ferromagnetic to superparamagnetic to paramagnetic—remains consistent across the range of M_{FM}. This confirms that the exact choice of M_{FM} within this range is not critical for the primary conclusions of our study.

We have thus fitted the M–H curves with $M_{FM} = 2\mu_B$ as shown in Fig. 3(a). In Fig. 3(b), we have plotted P_{FM}, P_{PM}, P_{SPM}, and P_{NM} as functions of temperature. Here, P_{NM} is the fraction of NM Mn ions, satisfying the relation $P_{FM} + P_{PM} + P_{SPM} + P_{NM} = 1$. Above T_C, the FM correlation length, namely, the size of SPM clusters represented by μ, is suppressed by thermal effects at high temperatures. As the temperature decreases, the fraction of PM and NM Mn ions gradually diminishes, while the fraction of SPM Mn ions increases. The large error bars in the high-temperature region suggest the presence of complex interactions and thermal effects that are not fully captured by the present model. Below T_C, as the temperature decreases further, P_{PM} and P_{NM} continue to decline, while P_{SPM} ceases to decrease, and a finite P_{FM} emerges and increases rapidly. At 35 K, a sudden change is observed in P_{FM} and P_{SPM}. This indicates that at this temperature, a sufficient number of ferromagnetic clusters break into smaller superparamagnetic clusters, resulting in a corresponding decrease in P_{FM} and an increase in P_{SPM}. Below 35 K, about 35% of Mn ions are distributed in the FM region, suggesting that $(Ba,K)(Zn,Mn)_2As_2$ has a potential to possess a FM fraction comparable to GaMnAs although the average FM moment per Mn ion is smaller than GaMnAs. In Fig. 3(c), we have plotted the average total magnetic moment of the SPM cluster μ against T. μ has a relatively temperature-independent large value of $\sim 200\mu_B$ below ~ 100 K. From this plot, we find that the average size of the SPM cluster is almost temperature independent at least below ~ 100 K.

We note that the M–H slope at 35 K differs from neighboring temperatures, which corresponds to irregularities in the fitted fractions in Figs. 3(b) and 3(c). Increasing error bars alone cannot reproduce this slope change, suggesting a nonstatistical origin. Elucidating its microscopic cause will require denser temperature sampling and is left for future work.

IV. DISCUSSION

We summarize the magnetization process of $(Ba,K)(Zn,Mn)_2As_2$ in the schematic picture of Fig. 4. The doped Mn ions are not uniformly distributed but some of the Mn ions are close to each other to form FM regions, SPM clusters, or nonmagnetic spin pairs. At high temperatures, FM exchange interaction between Mn ions is not able to align the spins of all the Mn ions and form SPM clusters. As the temperature decreases, the FM correlation between Mn ions becomes relatively long ranged, and simultaneously the number of nanoscale clusters increases, which leads to superparamagnetism [35].

In GaMnAs, Mn^{2+} simultaneously supplies local spins and holes, leading to hole-mediated long-range ferromagnetism in which AFM coupling does not occur for any Mn–Mn distance [36]. In contrast, for the 122-type $(Ba,K)(Zn,Mn)_2As_2$, first-principles calculations indicate that the nearest-neighbor Mn–Mn interaction is antiferromagnetic due to distinct Mn–As–Mn bonding geometry and exchange pathways [25]. This key difference rationalizes the reduced effective moments of SPM clusters in our analysis and the necessity to include an AFM-related nonmagnetic (P_{NM}) fraction in the fitting.

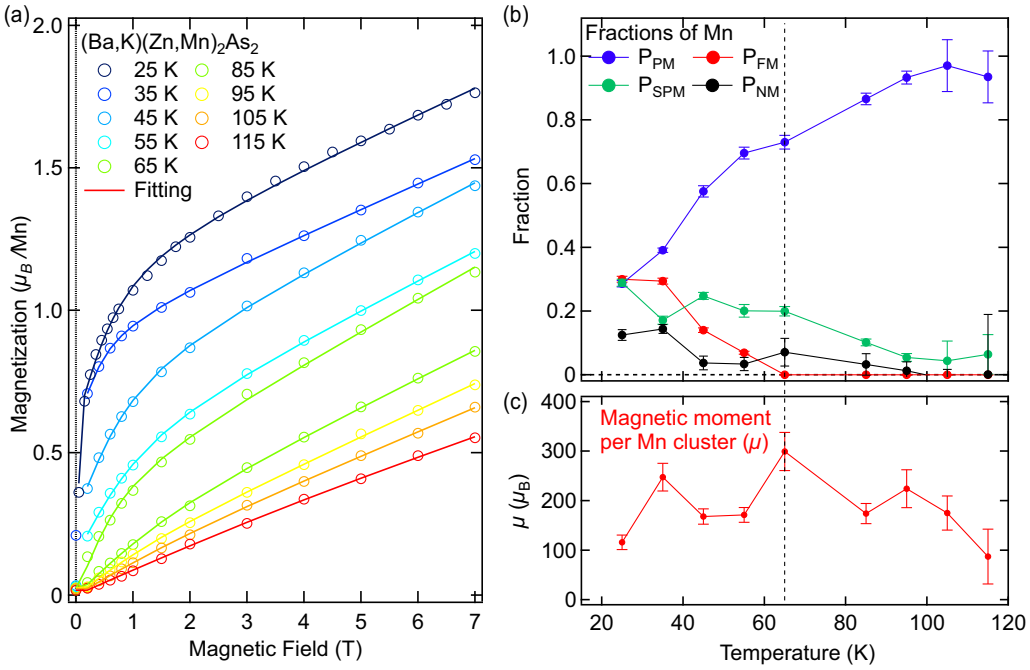

FIG. 3. Fitting results for M–H curves of $(Ba_{0.904}K_{0.096})(Zn_{0.805}Mn_{0.195})_2As_2$ at various temperatures and fitting parameters. (a) M–H curves deduced from the Mn L_3-edge XMCD. The circles are experimental data and the solid lines are fitting results. (b) Fractions of superparamagnetic (SPM), paramagnetic (PM), ferromagnetic (FM), and nonmagnetic (NM) ions, denoted by P_{SPM}, P_{PM}, P_{FM}, and P_{NM}, respectively. (c) Total magnetic moment per FM/SPM cluster μ. Here $\mu = \chi_{SPM} k_B T$. The vertical dashed line indicates the Curie temperature $T_C \sim 60$ K of the sample.

It should be noted that at high temperatures, this model may not fully account for the complex interactions and thermal effects, and because variation of M_{FM} with temperature is neglected. The model could be improved by incorporating a reliable estimation of the temperature dependence of M_{FM}. Another potential improvement could involve applying weighting to the Mn ion distribution across different field regions, which may improve the fit quality.

Along with the RPES and ARPES results of Suzuki *et al.* [27,28], the magnetization process observed in the present work proves that the FM properties of $(Ba,K)(Zn,Mn)_2As_2$ are governed by the competing FM and AFM interaction between the spins of localized Mn $3d$ electrons. Because in $(Ba,K)(Zn,Mn)_2As_2$, the carrier and spin densities can be controlled independently by doping at different sites, the chemical potential can be controlled more freely than in GaMnAs. The ARPES study suggests that, in $(Ba,K)(Zn,Mn)_2As_2$, the As $4p$ band, which is hybridized with Mn $3d$, forms Fermi surfaces and that the impurity band is formed below the Fermi level and hence below the valence-band maximum [28]. This is contrasted with GaMnAs, where the impurity band is located above the As $4p$-derived valence band maximum and pins the Fermi level [18]. Thus, in $(Ba,K)(Zn,Mn)_2As_2$, the Fermi

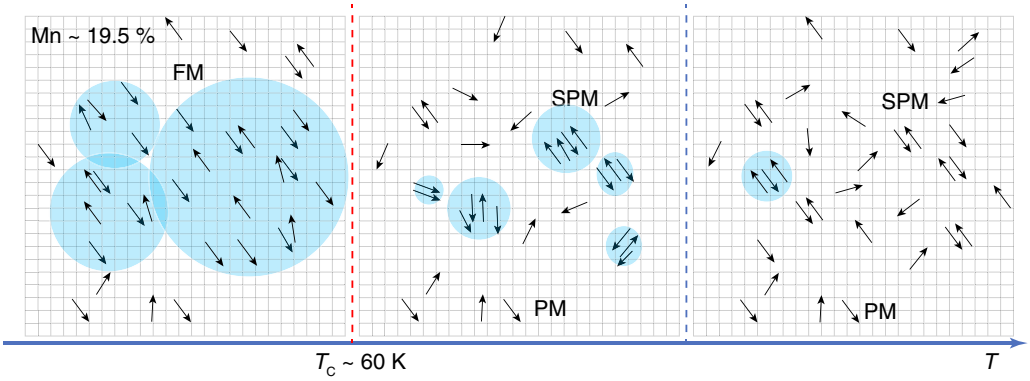

FIG. 4. Schematic illustration of the magnetization process in $(Ba,K)(Zn,Mn)_2As_2$. Paramagnetic isolated Mn ions, along with SPM and FM Mn-rich clusters, characterize the magnetic properties of the material. However, Mn spins within each SPM cluster are not fully aligned due to nearest-neighbor AFM interactions. As the temperature decreases, the SPM clusters interconnect to form larger SPM clusters and eventually evolve into FM regions below T_C. The sizes of the SPM clusters are not necessarily uniform.

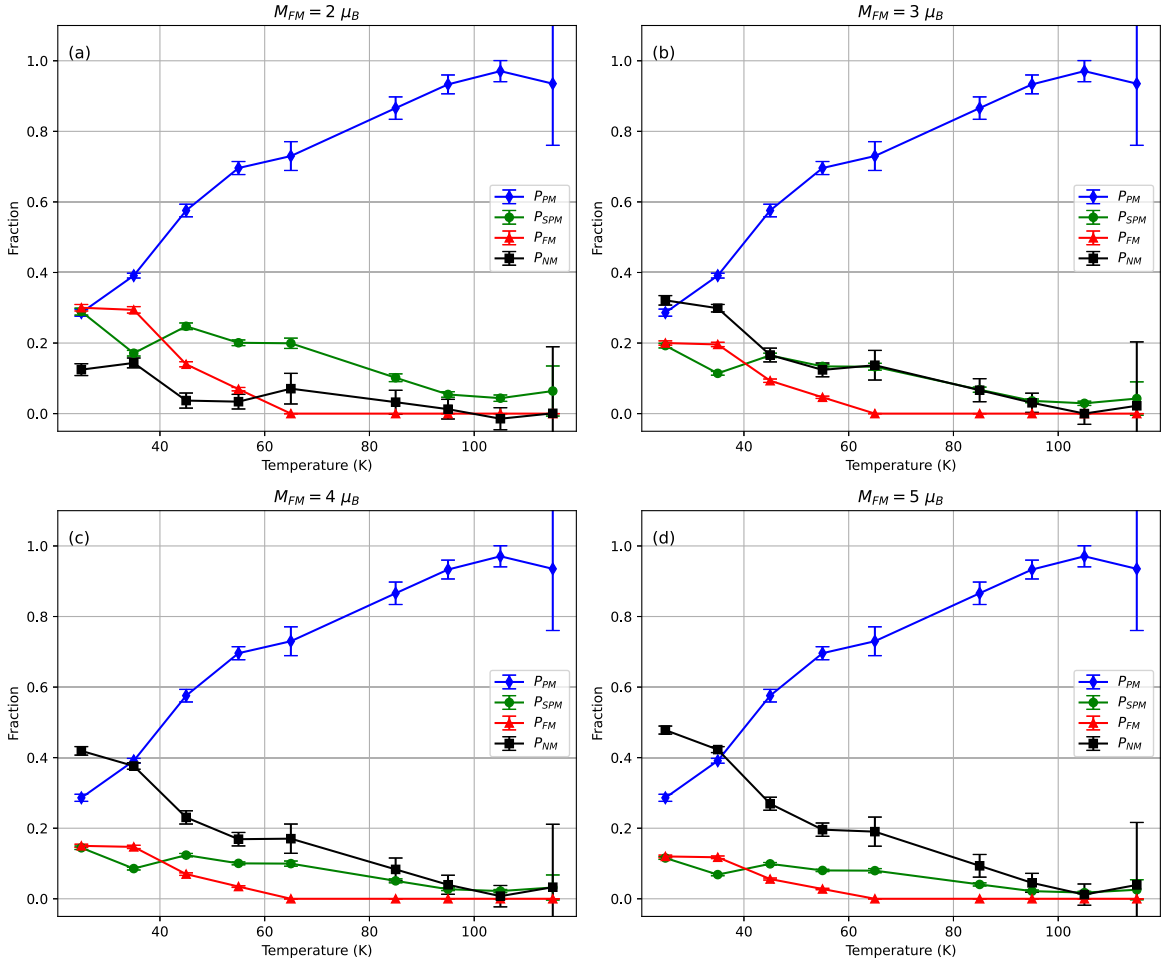

FIG. 5. Fractions of superparamagnetic (SPM), paramagnetic (PM), ferromagnetic (FM), and nonmagnetic (NM) ions, denoted by P_{SPM}, P_{PM}, P_{FM}, and P_{NM}, respectively, for M_{FM} values varying from 2 to $5\mu_B$. The trends are consistent with those shown in Fig. 3(b) of the main manuscript, demonstrating the robustness of the observed cluster evolution regardless of the chosen M_{FM}.

surfaces contribute to the metallic properties and mediate the ferromagnetic interaction between the Mn spins. In spite of these differences in their electronic structures, the magnetization behaviors of $(Ba,K)(Zn,Mn)_2As_2$ is similar to GaMnAs in several aspects [32].

V. CONCLUSION

We investigated the magnetization process of the FMS $(Ba,K)(Zn,Mn)_2As_2$ at various temperatures using magnetic field dependent XMCD measurements at the $L_{2,3}$ edges of the doped magnetic Mn^{2+} ions. We found that the magnetization process consists of the superparamagnetic (SPM), ferromagnetic (FM), and paramagnetic (PM) components. Nanoscale magnetic clusters contribute to the superparamagnetism, and the interconnected SPM clusters contribute to the ferromagnetism. Isolated Mn ions contribute to the PM component even below the Curie temperature. We also conclude that short-range AFM coupling exists between nearest-neighbor Mn ions in the FM region and SPM clusters, and is responsible for the different magnetic properties between $(Ba,K)(Zn,Mn)_2As_2$ and GaMnAs. The present XMCD studies, along with the previous photoemission studies, explain the origin of the magnetism in this kind of high T_C FMS [37]. The improved fitting method employed here can also be widely used in studying the magnetization processes of other magnetic materials. $(Ba,K)(Zn,Mn)_2As_2$ is a good platform to study dilute ferromagnetism in FMS and has high potential for FMS materials with highly controllable physical properties.

ACKNOWLEDGMENTS

This work was supported by Grants-in-Aid for Scientific Research from JSPS (S22224005, JP15K17696, JP19K03741, JP20K14416, and JP22K03535), Spintronics Research Network of Japan (Spin-RNJ), Reimei Project from Japan Atomic Energy Agency, Nanotechnology Platform (Project No. 12024606) of the MEXT, Friends of Todai Foundation in New York, the US NSF PIRE (Partnership for International Research and Education: OISE-0968226), and the US National Science Foundation Grant No. DMR-1610633. Measurements were performed under the Shared Use Program of Japan Atomic Energy Agency (JAEA) Facilities (Proposal No. 2017B-E19) supported by JAEA Advanced Characterization Nanotechnology Platform as a program of "Nanotechnology Platform" of the Ministry of Education, Culture, Science and Technology (MEXT)

TABLE II. Representative fitted fractions at 25, 65, and 105 K with $M_{FM} = 2\mu_B$. Numbers in parentheses denote 1σ uncertainties in the last digits. Fractions were constrained to $P_{FM} = 0$ for $T \geqslant 65$ K (see footnote [a]). Rows may not sum exactly to 1 because of rounding and constraints.

T (K)	P_{FM}	P_{SPM}	P_{PM}	P_{NM}
25	0.300(9)	0.289(10)	0.286(10)	0.125(17)
65	0.000[a]	0.199(15)	0.730(41)	0.071(43)
105	0.000[a]	0.044(9)	0.971(30)	0.000(31)[b]

[a]Parameter was fixed by the fitting model for $T \geqslant 65$ K (not a free fit result).

[b]Central fit value at 105 K was slightly negative [−0.014(31)]; it is reported here as 0.000(31) to reflect physical non-negativity while preserving the uncertainty.

(Proposal No. A-17-AE-0038). The synchrotron radiation experiments were performed at the JAEA beamline BL23SU in SPring-8 (Proposal No. 2017B3841). A.F. acknowledges the support of the National Science and Technology Council of Taiwan under Grant No. 113-2112-M-007-033 and the Yushan Fellow Program and the Center for Quantum Science and Technology within the framework of the Higher Education Sprout Project under the Ministry of Education of Taiwan. Y.W. acknowledges financial support from the Advanced Leading Graduate Course for Photon Science (ALPS).

APPENDIX A: ROBUSTNESS OF FITTING RESULTS WITH VARYING M_{FM}

We investigated the dependence of extracted model parameters on the value of M_{FM}. Figure 5 shows the fractions of superparamagnetic (P_{SPM}), paramagnetic (P_{PM}), ferromagnetic (P_{FM}), and nonmagnetic (P_{NM}) Mn^{2+} ions for M_{FM} values ranging from 2 to $5\mu_B$. These results demonstrate that, while the absolute values of P_{SPM}, P_{PM}, P_{FM}, and P_{NM} vary depending on M_{FM}, the overall trends remain consistent. Specifically, the evolution of magnetic clusters with increasing temperature—from ferromagnetic to superparamagnetic to paramagnetic—exhibits the same qualitative temperature dependences regardless of the chosen M_{FM}.

APPENDIX B: REPRESENTATIVE FITTED FRACTIONS AT SELECTED TEMPERATURES

The representative fitted fractions at selected temperatures are summarized in Table II.

[1] S. A. Wolf, D. D. Awschalom, R. A. Buhrman, J. M. Daughton, S. Von Molnár, M. L. Roukes, A. Y. Chtchelkanova, and D. M. Treger, Spintronics: A spin-based electronics vision for the future, Science **294**, 1488 (2001).

[2] I. Žutić, J. Fabian, and S. D. Sarma, Spintronics: Fundamentals and applications, Rev. Mod. Phys. **76**, 323 (2004).

[3] T. Dietl, Origin of ferromagnetic response in diluted magnetic semiconductors and oxides, J. Phys.: Condens. Matter **19**, 165204 (2007).

[4] T. Dietl, A ten-year perspective on dilute magnetic semiconductors and oxides, Nat. Mater. **9**, 965 (2010).

[5] H. Ohno, H. Munekata, T. Penney, S. Von Molnar, and L. L. Chang, Magnetotransport properties of *p*-type (In, Mn) As diluted magnetic III-V semiconductors, Phys. Rev. Lett. **68**, 2664 (1992).

[6] H. Ohno, A. Shen, F. Matsukura, A. Oiwa, A. Endo, S. Katsumoto, and Y. Iye, (Ga,Mn)As: A new diluted magnetic semiconductor based on GaAs, Appl. Phys. Lett. **69**, 363 (1996).

[7] F. Matsukura, H. Ohno, A. Shen, and Y. Sugawara, Transport properties and origin of ferromagnetism in (Ga, Mn) As, Phys. Rev. B **57**, R2037 (1998).

[8] Y. Takeda, M. Kobayashi, T. Okane, T. Ohkochi, J. Okamoto, Y. Saitoh, K. Kobayashi, H. Yamagami, A. Fujimori, A. Tanaka, J. Okabayashi, M. Oshima, S. Ohya, P. N. Hai, and M. Tanaka, Nature of magnetic coupling between Mn ions in as-grown $Ga_{1-x}Mn_xAs$ studied by x-ray magnetic circular dichroism, Phys. Rev. Lett. **100**, 247202 (2008).

[9] C. Zener, Interaction between the *d* shells in the transition metals, Phys. Rev. **81**, 440 (1951).

[10] C. Zener, Interaction between the *d*-shells in the transition metals. II. ferromagnetic compounds of manganese with perovskite structure, Phys. Rev. **82**, 403 (1951).

[11] T. Dietl, A. Haury, and Y. Merle d'Aubigné, Free carrier-induced ferromagnetism in structures of diluted magnetic semiconductors, Phys. Rev. B **55**, R3347 (1997).

[12] T. Dietl, H. Ohno, F. Matsukura, J. Cibert, and D. Ferrand, Zener model description of ferromagnetism in zinc-blende magnetic semiconductors, Science **287**, 1019 (2000).

[13] T. Jungwirth, J. Sinova, A. H. MacDonald, B. L. Gallagher, V. Novák, K. W. Edmonds, A. W. Rushforth, R. P. Campion, C. T. Foxon, L. Eaves, E. Olejník, J. Mašek, S. R. E. Yang, J. Wunderlich, C. Gould, L. W. Molenkamp, T. Dietl, and H. Ohno, Character of states near the Fermi level in (Ga,Mn)As: Impurity to valence band crossover, Phys. Rev. B **76**, 125206 (2007).

[14] M. Berciu and R. N. Bhatt, Effects of disorder on ferromagnetism in diluted magnetic semiconductors, Phys. Rev. Lett. **87**, 107203 (2001).

[15] A. Kaminski and S. Das Sarma, Polaron percolation in diluted magnetic semiconductors, Phys. Rev. Lett. **88**, 247202 (2002).

[16] P. Mahadevan and A. Zunger, Trends in ferromagnetism, hole localization, and acceptor level depth for Mn substitution in GaN, GaP, GaAs, and GaSb, Appl. Phys. Lett. **85**, 2860 (2004).

[17] J. Coey, M. Venkatesan, and C. Fitzgerald, Donor impurity band exchange in dilute ferromagnetic oxides, Nat. Mater. **4**, 173 (2005).

[18] M. Kobayashi, I. Muneta, Y. Takeda, Y. Harada, A. Fujimori, J. Krempaský, T. Schmitt, S. Ohya, M. Tanaka, M. Oshima, and V. N. Strocov, Unveiling the impurity band induced ferromagnetism in the magnetic semiconductor (Ga,Mn)As, Phys. Rev. B **89**, 205204 (2014).

[19] C. T. Foxon, R. P. Campion, K. W. Edmonds, L. Zhao, K. Wang, N. R. Farley, C. R. Staddon, and B. L. Gallagher, The growth of high quality GaMnAs films by MBE, J. Mater. Sci.: Mater. Electron. **15**, 727 (2004).

[20] J. Sadowski and J. Z. Domagala, Influence of defects on the lattice constant of GaMnAs, Phys. Rev. B **69**, 075206 (2004).

[21] K. M. Yu, W. Walukiewicz, T. Wojtowicz, I. Kuryliszyn, X. Liu, Y. Sasaki, and J. K. Furdyna, Effect of the location of Mn sites in ferromagnetic $Ga_{1-x}Mn_xAs$ on its Curie temperature, Phys. Rev. B **65**, 201303(R) (2002).

[22] K. Zhao, Z. Deng, X. C. Wang, W. Han, J. L. Zhu, X. Li, Q. Q. Liu, R. C. Yu, T. Goko, B. Frandsen, L. Liu, F. Ning, Y. J. Uemura, H. Dabkowska, G. M. Luke, H. Luetkens, E. Morenzoni, S. R. Dunsiger, A. Senyshyn, P. Böni, *et al.*, New diluted ferromagnetic semiconductor with Curie temperature up to 180 K and isostructural to the "122" iron-based superconductors, Nat. Commun. **4**, 1442 (2013).

[23] J. Paglione and R. L. Greene, High-temperature superconductivity in iron-based materials, Nat. Phys. **6**, 645 (2010).

[24] G. Q. Zhao, C. J. Lin, Z. Deng, G. X. Gu, S. Yu, X. C. Wang, Z. Z. Gong, Y. J. Uemera, Y. Q. Li, and C. Q. Jin, Single crystal growth and spin polarization measurements of diluted magnetic semiconductor $(Ba,K)(Zn,Mn)_2As_2$, Sci. Rep. **7**, 14473 (2017).

[25] J. K. Glasbrenner, I. Žutić, and I. I. Mazin, Theory of Mn-doped II-II-V semiconductors, Phys. Rev. B **90**, 140403(R) (2014).

[26] Y. Peng, X. Li, L. Shi, G. Zhao, J. Zhang, J. Zhao, X. Wang, B. Gu, Z. Deng, Y. J. Uemura, *et al.*, A near room temperature Curie temperature in a new type of diluted magnetic semiconductor $(Ba,K)(Zn,Mn)_2As_2$, Adv. Phys. Res. **4**2400124 (2024).

[27] H. Suzuki, K. Zhao, G. Shibata, Y. Takahashi, S. Sakamoto, K. Yoshimatsu, B. J. Chen, H. Kumigashira, F. H. Chang, H. J. Lin, D. J. Huang, C. T. Chen, B. Gu, S. Maekawa, Y. J. Uemura, C. Q. Jin, and A. Fujimori, Photoemission and x-ray absorption studies of the isostructural to Fe-based superconductors diluted magnetic semiconductor $Ba_{1-x}K_x(Zn_{1-y}Mn_y)_2As_2$, Phys. Rev. B **91**, 140401(R) (2015).

[28] H. Suzuki, G. Q. Zhao, K. Zhao, B. J. Chen, M. Horio, K. Koshiishi, J. Xu, M. Kobayashi, M. Minohara, E. Sakai, K. Horiba, H. Kumigashira, B. Gu, S. Maekawa, Y. J. Uemura, C. Q. Jin, and A. Fujimori, Fermi surfaces and *p-d* hybridization in the diluted magnetic semiconductor $Ba_{1-x}K_x(Zn_{1-y}Mn_y)_2As_2$ studied by soft x-ray angle-resolved photoemission spectroscopy, Phys. Rev. B **92**, 235120 (2015).

[29] H. Suzuki, G. Zhao, J. Okamoto, S. Sakamoto, Z.-Y. Chen, Y. Nonaka, G. Shibata, K. Zhao, B. Chen, W.-B. Wu, F.-H. Chang, H.-J. Lin, C.-T. Chen, A. Tanaka, M. Kobayashi, B. Gu, S. Maekawa, Y. J. Uemura, C. Jin, D.-J. Huang, *et al.*, Magnetic properties and electronic configurations of Mn ions in the diluted magnetic semiconductor $Ba_{1-x}K_x(Zn_{1-y}Mn_y)_2As_2$ studied by x-ray magnetic circular dichroism and resonant inelastic x-ray scattering, J. Phys. Soc. Jpn. **91**, 064710 (2022).

[30] S. Sakamoto, G. Zhao, G. Shibata, Z. Deng, K. Zhao, X. Wang, Y. Nonaka, K. Ikeda, Z. Chi, Y. Wan, M. Suzuki, T. Koide, A. Tanaka, S. Maekawa, Y. Uemura, C. Jin, and A. Fujimori, Anisotropic spin distribution and perpendicular magnetic anisotropy in a layered ferromagnetic semiconductor $(Ba,K)(Zn,Mn)_2As_2$, ACS Appl. Electron. Mater. **3**, 789 (2021).

[31] S. Sakamoto, L. D. Anh, P. N. Hai, G. Shibata, Y. Takeda, M. Kobayashi, Y. Takahashi, T. Koide, M. Tanaka, and A. Fujimori, Magnetization process of the *n*-type ferromagnetic semiconductor (In,Fe)As:Be studied by x-ray magnetic circular dichroism, Phys. Rev. B **93**, 035203 (2016).

[32] Y. Takeda, S. Ohya, N. H. Pham, M. Kobayashi, Y. Saitoh, H. Yamagami, M. Tanaka, and A. Fujimori, Direct observation of the magnetic ordering process in the ferromagnetic semiconductor $Ga_{1-x}Mn_xAs$ via soft x-ray magnetic circular dichroism, J. Appl. Phys. **128**, 213902 (2020).

[33] Y. Saitoh, Y. Fukuda, Y. Takeda, H. Yamagami, S. Takahashi, Y. Asano, T. Hara, K. Shirasawa, M. Takeuchi, T. Tanaka, and H. Kitamura, Performance upgrade in the JAEA actinide science beamline BL23SU at SPring-8 with a new twin-helical undulator, J. Synchrotron Rad. **19**, 388 (2012).

[34] Y. Teramura, A. Tanaka, and J. O. Takeo, Effect of Coulomb interaction on the x-ray magnetic circular dichroism spin sum rule in 3d transition elements, J. Phys. Soc. Jpn. **65**, 1053 (1996).

[35] V. Demas and T. J. Lowery, Magnetic resonance for in vitro medical diagnostics: Superparamagnetic nanoparticle-based magnetic relaxation switches, New J. Phys. **13**, 025005 (2011).

[36] P. Mahadevan, A. Zunger, and D. D. Sarma, Unusual directional dependence of exchange energies in GaAs diluted with Mn: Is the RKKY description relevant? Phys. Rev. Lett. **93**, 177201 (2004).

[37] A. D. Bouravleuv, L. L. Lev, C. Piamonteze, X. Wang, T. Schmitt, A. I. Khrebtov, Y. B. Samsonenko, J. Kanski, G. E. Cirlin, and V. N. Strocov, Electronic structure of (In,Mn)As quantum dots buried in GaAs investigated by soft-x-ray ARPES, Nanotechnology **27**, 425706 (2016).